Title

Coherently aligned nanoparticles within a biogenic single crystal: A biological prestressing strategy

Journal

Science, 358(6368)

ISSN

0036-8075

Authors

Polishchuk, Iryna

Bracha, Avigail Aronhime

Bloch, Leonid

et al.

Publication Date

2017-12-08

DOI

10.1126/science.aaj2156

Peer reviewed

REPORT

BIOLOGICAL MATERIALS

Coherently aligned nanoparticles within a biogenic single crystal: A biological prestressing strategy

Iryna Polishchuk,[1]* Avigail Aronhime Bracha,[1]* Leonid Bloch,[1]† Davide Levy,[1] Stas Kozachkevich,[1] Yael Etinger-Geller,[1] Yaron Kauffmann,[1] Manfred Burghammer,[2] Carlotta Giacobbe,[2] Julie Villanova,[2] Gordon Hendler,[3] Chang-Yu Sun,[4] Anthony J. Giuffre,[4] Matthew A. Marcus,[5] Lakshminath Kundanati,[6] Paul Zaslansky,[7] Nicola M. Pugno,[6,8,9] Pupa U. P. A. Gilbert,[4] Alex Katsman,[1] Boaz Pokroy[1]‡

In contrast to synthetic materials, materials produced by organisms are formed in ambient conditions and with a limited selection of elements. Nevertheless, living organisms reveal elegant strategies for achieving specific functions, ranging from skeletal support to mastication, from sensors and defensive tools to optical function. Using state-of-the-art characterization techniques, we present a biostrategy for strengthening and toughening the otherwise brittle calcite optical lenses found in the brittlestar *Ophiocoma wendtii*. This intriguing process uses coherent nanoprecipitates to induce compressive stresses on the host matrix, functionally resembling the Guinier–Preston zones known in classical metallurgy. We believe that these calcitic nanoparticles, being rich in magnesium, segregate during or just after transformation from amorphous to crystalline phase, similarly to segregation behavior from a supersaturated quenched alloy.

Diverse functional materials are formed in the course of biomineralization. They provide skeletal support (*1*), mastication (*2*), gravity sensing (*3*) and magnetic sensing (*4*), defense tools (*5*), photoreception (*6*, *7*), and more, using limited bioavailable elements. Natural processes for strengthening mineralized materials include the incorporation of intracrystalline macromolecules within their crystalline lattices, which increase the hardness and fracture toughness of the host crystals (*8*). A second strategy is the formation of structures with several orders of hierarchical architecture (*9*, *10*), shown to enhance the mechanical properties of the often-brittle building materials. A third strategy derives from transient amorphous precursor (*11*) from which many biominerals are formed, and which among other benefits facilitate the formation of curved and intricately shaped single crystals (*12*). A fourth finding is that biominerals often possess multifunctionality, allowing one material to exhibit several functions in parallel (*7*, *13*). Here we present another biostrategy, for toughening brittle single crystals of calcite.

Our studies of the atomic- and nanostructure of the dorsal arm plates of the brittlestar *Ophiocoma wendtii* (fig. S1) disclose the presence of coherent nanoprecipitates that induce comprehensive compressive stresses on the host single crystal, akin to the Guinier–Preston zones known in classical metallurgy (*14*). The arm plates of these brittlestars (*15*) are covered by hundreds of calcite lenses, each several tens of micrometers in size (*16*, *17*). The lenses were found to be part of a large single crystal, with microlenses that focus light onto photoreceptor nerve bundles positioned beneath them. Each lens is aligned along its optical axis parallel to the *c* axis of calcite. This orientation minimizes the effect of the birefringence of calcite, preventing double vision.

Lenses (Fig. 1A) have curved surfaces that focus light on the presumed photoreceptors (*16*, *17*). Examination of the dorsal arm plates by high-resolution powder x-ray diffraction (HRPXRD) (*15*) (Fig. 2A) revealed the structure of calcite only. After Rietveld refinement analysis, we obtained lattice parameters smaller than those of pure calcite, but very close in size to those expected from magnesium substitution (*18*): a = 4.92577(3) Å and c = 16.76897(6) Å (table S3). Measurement of the magnesium content and other impurities by means of inductively coupled plasma optical emission spectroscopy (ICP-OES), electron probe microanalysis (EPMA), and energy-dispersive spectroscopy (*15*) revealed an average concentration, η_{avg}, of about 15.2 ± 0.1 mol %, where η = Mg/(Ca + Mg) mol % (tables S1 and S2) (*15*). Magnesium readily substitutes for calcium in the calcite structure and causes the lattice parameters to shrink (*19*).

Typical bright-field aberration–corrected high-resolution transmission electron microscopy (HRTEM) images can be seen in Fig. 1, B and C. Even though the entire dorsal arm plate has been identified as a calcite single crystal, an ensemble of nanodomains can be observed within the matrix (Fig. 1, B and C). These nanodomains appear brighter in bright-field mode, indicating their relatively lower electron density. Despite the presence of these domains, fast Fourier transform (FFT) of the entire image on TEM yields a single-crystal pattern (Fig. 1, B and C, insets). On the likely assumption that the *O. wendtii* lenses are formed via transient amorphous precursors, as are other echinoderm ossicles (*11*), we explored the possibility that these nanodomains consist of residual amorphous material. This was ruled out, however, by differential scanning calorimetry coupled with thermal gravimetric analysis, which did not show any of the exothermal peaks (fig. S2) that are observed when amorphous calcium carbonate is heated and crystallized.

We further subjected powdered dorsal arm plates, while they were undergoing HRPXRD, to isochronous heating in situ at 30-min intervals at various temperatures up to 650°C. Upon heating, the diffraction peaks showed a large but gradual shift to lower diffraction angles (Fig. 2C) opposite in sign to that of the shift observed for other annealed biogenic calcites (*19*). After treatment at 650°C, the lens's lattice reverted to a calcite-like lattice with a median magnesium concentration of about 0.4 mol %. After annealing at 400°C, a new calcite nanoscale phase appeared, with lattice parameters a = 4.837(1) Å and c = 16.155(2) Å (Fig. 2C and table S3). The emergence of this nanophase was accompanied by a strong shift in peak position of the main calcite matrix. The lattice parameters of the calcite nanophase corresponded to a magnesium-rich phase with a magnesium concentration of η_p ~ 40 mol %. This nanophase is identical to that of the nanoparticles seen in the TEM imaging (Fig. 1, B to D), and their brighter appearance in bright-field TEM is explained by the presence of magnesium-rich calcite. Moreover, upon high-angle annular dark field (HAADF) scanning TEM, which provides *z*-contrast imaging, these nanodomains appear darker than the matrix, confirming a lower average atomic number, as expected for magnesium-rich particles in a calcium-rich matrix (fig. S3).

Samples were heated in situ within the TEM, which induced crystal growth. The nanoparticles grew from several nanometers to about 20 to 40 nm at 450°C (Fig. 1D). Line-profile analysis of

[1]Department of Materials Science and Engineering and the Russel Berrie Nanotechnology Institute, Technion-Israel Institute of Technology, 32000 Haifa, Israel. [2]The European Synchrotron, CS 40220, 38043 Grenoble Cedex 9, France. [3]Natural History Museum of Los Angeles County, Los Angeles, CA 90007, USA. [4]Departments of Physics, Chemistry, Geoscience, University of Wisconsin–Madison, Madison, WI 53706, USA. [5]Advanced Light Source, Lawrence Berkeley National Laboratory, Berkeley, CA 94720, USA. [6]Laboratory of Bio-Inspired and Graphene Nanomechanics, Department of Civil, Environmental and Mechanical Engineering, University of Trento, Via Mesiano 77, 38123 Trento, Italy. [7]Department for Restorative and Preventive Dentistry, Centrum für Zahn-, Mund- und Kieferheilkunde, Charité–Universitätsmedizin Berlin, 14197 Berlin, Germany. [8]School of Engineering and Materials Science, Queen Mary University of London, Mile End Road, London E1 4NS, UK. [9]Ket-Lab, Edoardo Amaldi Foundation, Italian Space Agency, Via del Politecnico snc, 00133 Rome, Italy. *These authors contributed equally to this work. †Present address: The European Synchrotron, CS 40220, 38043 Grenoble Cedex 9, France, and Institute of Technology in Zurich, Rämistrasse 101, 8092 Zürich, Switzerland.
‡Corresponding author. Email: bpokroy@technion.ac.il

the powder x-ray diffraction (XRD) corroborated this finding (fig. S4). Magnesium energy-filtered TEM of the heated sample confirmed that the domains were magnesium-rich when compared to the matrix (fig. S5). Proof that the domains are rich in magnesium was obtained, before heat treatment, by x-ray absorption near-edge structure spectroscopy and photoemission electron microscopy (XANES-PEEM) (*15*) (Fig. 3, A and B) and by two-dimensional (2D) time-of-flight secondary ion mass spectrometry (ToF-SIMS) (*15*) from a single lens (Fig. 3C). Both assessments revealed that the dispersed particles are richer in magnesium than the matrix. Component mapping with PEEM (*15*) was possible because the nanodomains and the lens matrix are spectroscopically distinct, as shown in XANES spectra (Fig. 3B and table S2).

As the calcite nanodomains are rich in magnesium, and the lattice parameters of these nanoparticles are considerably smaller than those of the calcite matrix, it would seem that at least part of the large shifts in diffraction peaks upon heating to larger lattice parameters is indicative of compressive strains in the crystal matrix. This is probably a result of coherence between the nanodomains and the matrix. The presence of local strain fields is confirmed by dark-field TEM imaging, in which strain fringes are seen (Fig. 1E); however, they completely disappear after heat treatment as the strains are relaxed (fig. S6).

We also performed submicrometer synchrotron scanning x-ray diffractometry (*15*) on cross sections of intact lens arrays, using a beam spot size of ~180 nm by 150 nm. Not only did this procedure verify that the entire lens array is a single crystal (see fig. S7), but we could also observe local variations of ±0.1% in the lattice parameters, as can be seen from the maps of the various *d* spacings (Fig. 4A).

The strengthening and toughening of these otherwise brittle lenses depends upon coherent magnesium-rich calcite nanoparticles within a lower-magnesium single crystal of calcite. These nanoparticles exert compressive strains on the matrix but are themselves under a high tensile strain. Because of the coherent interface before heat treatment, the presence of two distinct phases is not detectable on HRPXRD. However, if the diffractogram is plotted with the intensity in logarithmic scale, a hump can be observed at the base of each of the diffraction peaks before annealing (Fig. 2, A and B). Line-profile analysis yields a nanoparticle size of about 5 nm. As the sample is heated and the particles grow, the coherent interface is eventually destroyed. The nanoparticles are very similar to those in coherent Guinier–Preston zones of classical metallurgy, which are formed by rapid cooling of a homogeneous alloy, with limited solubility of one of the components at low temperatures. After quenching, the system is out of phase equilibrium and in a supersaturated solid solution state. As a result, and owing to the low rate of diffusion at ambient temperature, coherent nanoprecipitates form in the matrix in a process termed "aging" and exert strains.

We believe that the brittlestar lens demonstrates a very similar strategy. The $CaCO_3$–$MgCO_3$ binary phase diagram reveals limited solubility of Mg

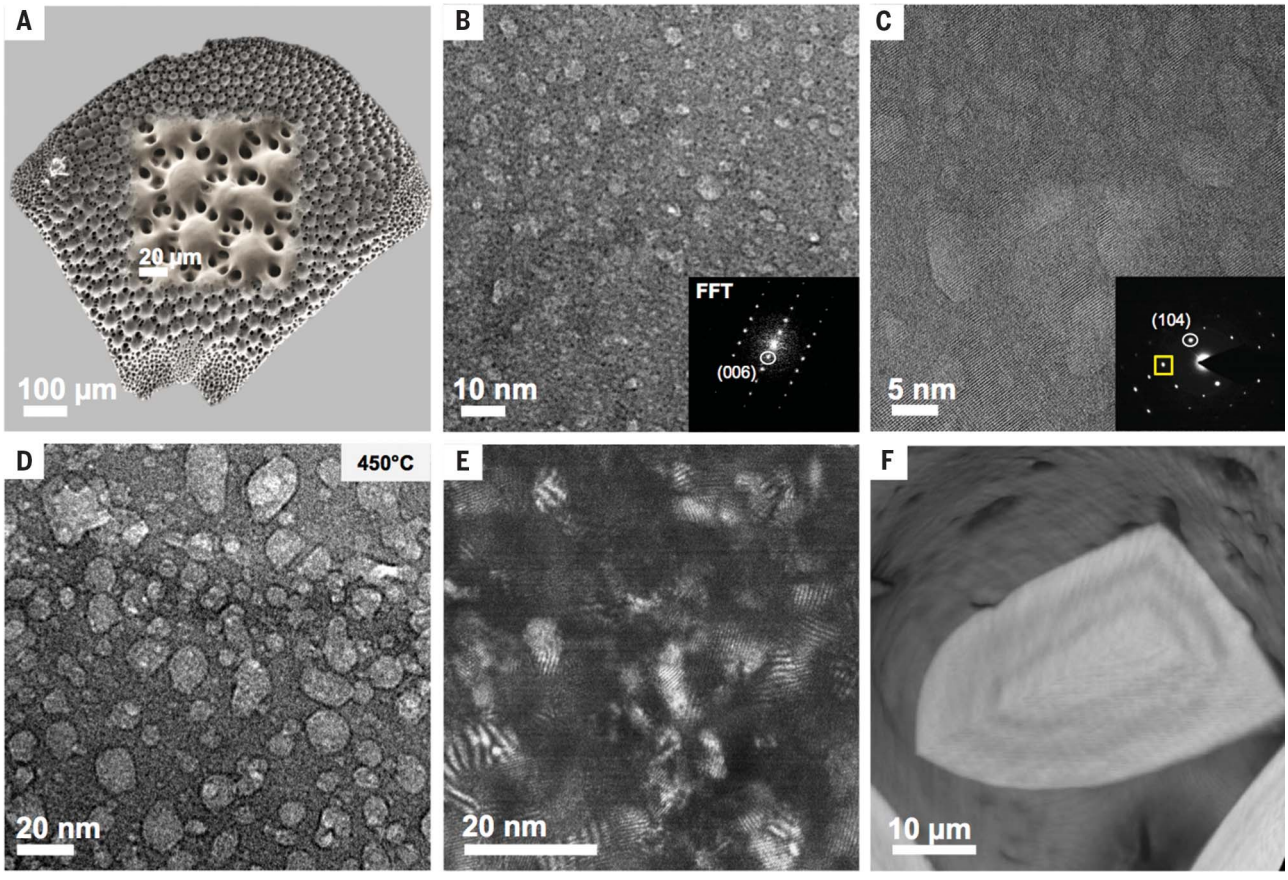

Fig. 1. Characterization from the micro- to the nanostructure. (**A**) Scanning electron microscopy image showing an entire dorsal arm plate and a higher-magnification inset. (**B**) HRTEM (*15*) image of a thin section from a lens revealing brighter nanodomains, although the FFT pattern (inset) is that of a single crystal. (**C**) Higher magnification of an area in (B) shows a lattice image undisrupted by the nanodomains, which demonstrate coherent interfaces with the lattice by the continuous lattice fringes. The inset shows an electron diffraction image from this area. (**D**) Bright-field TEM image obtained during in situ heating at 450°C, revealing the temperature-dependent growth of the nanodomains. (**E**) Dark-field HRTEM acquired using the diffracted beam marked by the diffraction spot in the yellow square in (C), and demonstrating numerous strain fringes. (**F**) A virtual slice within a single lens produced by 3D x-ray nanoCT (*15*), revealing alternating density layers probably owing to varying nanoprecipitate content.

(up to only a few Mg percent) in calcite at room temperature, after which dolomite is precipitated (*20*). It is reasonable to assume that the amorphous precursor is utilized in vivo as an alternative route to form supersaturated solid solutions (*11*), which allow for some precipitation of magnesium-rich calcium carbonate during or after crystallization.

Quantitative XRD data analysis of the heated samples reveals a volume fraction of ~8% magnesium-rich phase. This concentration may seem too low to exert coherent strains on the entire matrix; however, if we consider a simple case in which the precipitates are spherical with a radius of r_0, then the distance between particles, l, is determined by their volume fraction, ϕ: $l = r_0(4\pi/3)^{1/3}$. For ϕ = 0.06, the distance $l = 4r_0$ (see fig. S8) and the distance between particle is only $2r_0$. On the basis of TEM and XRD, we can estimate $2r_0$ to be ~5 nm. Bearing in mind that the strain caused by an isolated spherical coherent inclusion in the matrix decreases with distance according to the law $(r_0/r)^3$, the average strain of the matrix caused by the ensemble of coherent inclusions can be estimated as $3Z(q^3-1)^{-1}\ln q\Delta\varepsilon^c_{ij}$, where $\Delta\varepsilon^c_{ij}$ is the maximum coherent strain near the inclusion/matrix interface, $q = l/r_0$, and Z is the coordination number of a precipitate (we used Z = 6). If the precipitate volume fraction ϕ ~ 0.08, the average coherent strain of the matrix may reach a magnitude of ~$0.5\Delta\varepsilon^c_{ij}$. The average macroscopic strain in a stress-free bulk crystal containing a homogeneous distribution of coherent magnesium-rich inclusions is $\overline{\varepsilon_{kl}} = \varepsilon^0_{kl}\phi$, where ε^0_{kl} is the stress-free strain of the inclusion phase (transformation strain). This macroscopic strain consists of elastic and inelastic components. Inelastic strain caused by transformation strain of inclusions, ε^0_{kl}, can be accompanied by substantial internal coherent strains, with corresponding tensile stresses in the particles and compressive stresses in the matrix (*15*). Because of the small particle size, the particles can withstand relatively large tensile stresses against coherence loss. As known from metallurgical Guinier–Preston zones, the stresses arise owing to the presence of coherent interfaces (*21*). When a growing coherent inclusion reaches a certain critical size, the elastic energy becomes high enough to induce relaxation processes, and the coherence is lost (*21*). The nanoparticles' critical size for coherence loss is evaluated from 20 to 40 nm (*15*). This is shown in Fig. 2C, where the nanoparticles grow while at the same time, the strains in the particles (tensile) and in the matrix (compressive) are relaxed.

To estimate the absolute strain in the matrix, it is necessary to know the magnesium concentrations in both the matrix and the nanoparticles to derive their elastic constants and the difference in their lattice parameters that leads to the lattice mismatch. If we assume that for nanoparticles, ϕ = 8%, and that their composition is close to 40 mol % magnesium, this yields a matrix concentration of η_{matrix} = 13.3(1) mol % magnesium [$\eta_{avg} = \phi\eta_p + (1-\phi)\eta_{matrix}$]. Using a Mori-Tanaka homogenization scheme (*22*), we evaluated the average hydrostatic elastic strain within the nanoparticles as ~2.3% and within the matrix ~−0.1%. These coherent strains may result in an average compressive hydrostatic stress of ~−170 MPa in the matrix (*15*). At first glance, these figures appear to be high; however, if we consider the precipitate size to be ~5 nm, we can conclude that the strain state is very similar to that of a thin epitaxial layer that often contains misfits of this order even for calcium carbonate (*23*).

When the TEM imaging is observed from different orientations, the nanoprecipitates appear to have a platelet-like shape (fig. S9). This is confirmed by the small-angle x-ray scattering (SAXS) (*15*) signal that was derived from submicrometer scanning diffractometry and revealed streak-shaped signals, supporting the platelet-like shape. Notably, an orientation of the SAXS signal is seen only in certain distinct layers within a single lens, but as the curved surface is approached, a strongly oriented streaklike SAXS signal can indeed be observed, indicating that the platelets are oriented with their flat surfaces parallel to the lens surface (Fig. 4, B and C, and movie S1).

This alignment is most probably attributable to surface image forces known to affect precipitate orientation, because the coherence strains are much more readily relaxed at the free surface of a crystal than at its interior. In addition, SAXS reveals ordered regions slightly beneath the curved surface in curved lines parallel to the surface (Fig. 4B). The same images also reveal a zone of lower SAXS intensity closer to the surface (Fig. 4B, green-blue color). This zone resembles a precipitate depletion zone that could correspond to what is known in metallurgy as a precipitate-free zone (*24*). In the composition field, such segregation sets up a fluctuation that is perpendicular to the free surface and that develops to form alternating magnesium-rich and magnesium-depleted layers parallel to the surface, a phenomenon known as surface-directed spinodal decomposition (*25*, *26*). Notably, observation of the lattice parameter map from the same lens (Fig. 4A) reveals alternating lattice parameters that correspond to the features observed by SAXS (Fig. 4B).

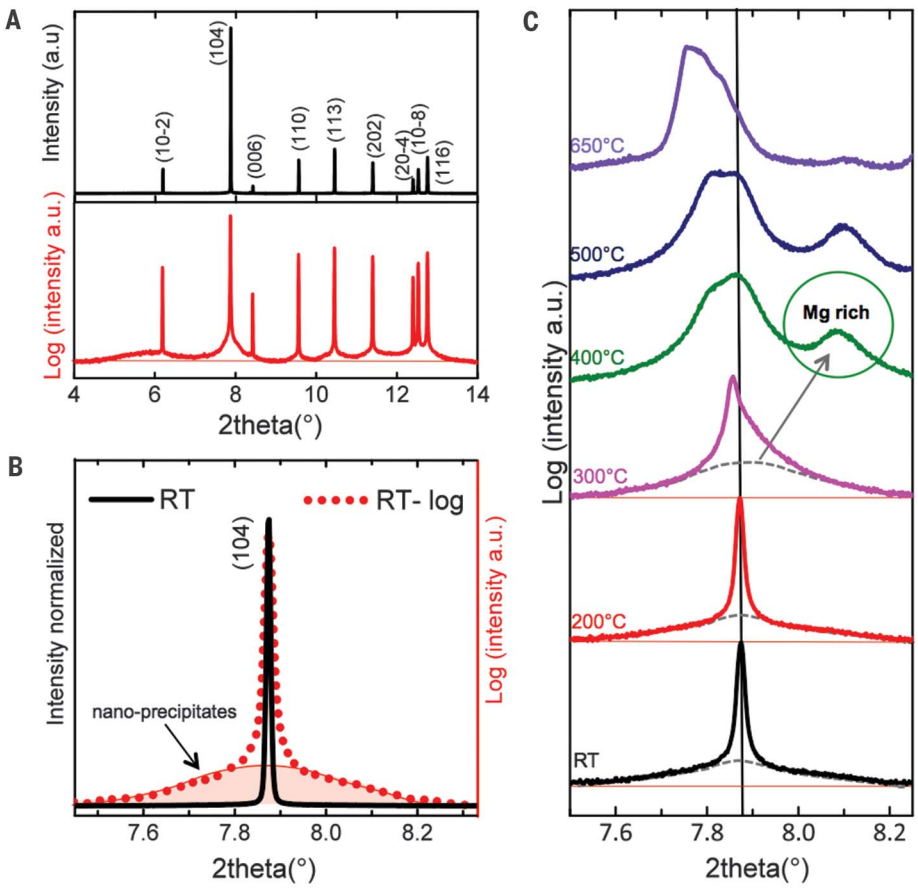

Fig. 2. High-resolution powder XRD characterization. (**A**) Full diffractogram of a powdered dorsal arm plates sample at room temperature collected at a wavelength of 0.4106 Å; linear intensity (black) and logarithmic intensity scales (red). (**B**) Enlargement of the (104) diffraction peak comparing linear (black) and logarithmic (red) intensity scales, and revealing the presence of nanodomains at the base of the diffraction peak. (**C**) Evolution of the (104) diffraction peak with heat treatments. After annealing at 400°C, a distinct broad diffraction peak appears owing to the heat-induced loss of nanoprecipitate coherence.

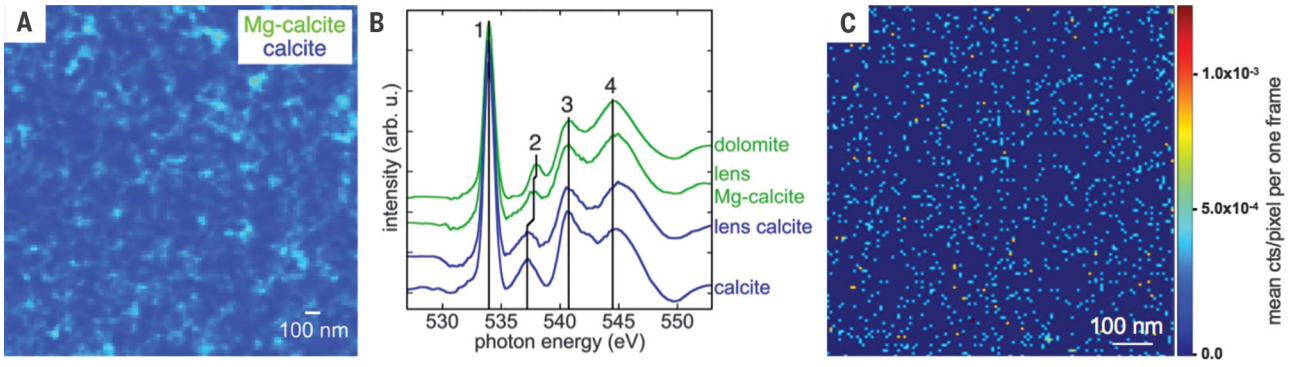

Fig. 3. PEEM and ToF-SIMS mapping. (**A**) PEEM component map with 20-nm pixels displaying the spatial distribution of the two phases in a brittlestar lens: low magnesium calcite (blue) and high magnesium calcite (green). Magnesium-rich calcite nanoparticles are only resolved as mixed with calcite (blue + green = cyan). (**B**) Oxygen XANES spectra show that lens calcite is similar to geological calcite, as shown by aligned peaks 1 to 4 (vertical lines, bottom). Lens Mg-calcite peak 2 is intermediate between calcite and dolomite. (**C**) Mg^+ distribution map acquired via ToF-SIMS analysis within a single lens. The map is 128 by 128 pixels, with 8 nm/pixel.

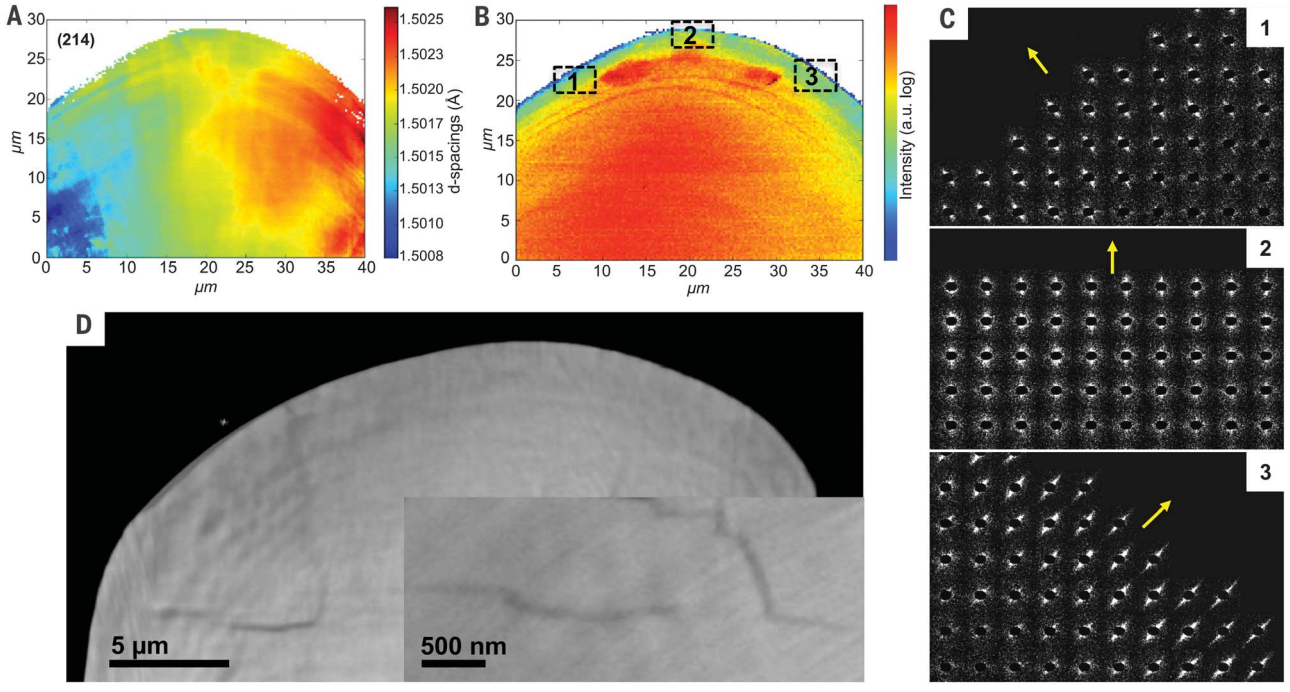

Fig. 4. Synchrotron submicrometer scanning diffraction and nanotomography. (**A**) A *d*-spacings map of a single lens area of the (214) reflection. (**B**) SAXS intensity map of the same lens (periodicities of ~2.5 to 16.5 nm). (**C**) SAXS signals from individual scanning positions reveal streaks elongated perpendicularly to the surface (yellow arrows). Numbering corresponds to the positions indicated in (B). (**D**) Nanotomographic map revealing alternating density layers. The inset (additional sample) shows a crack deflection resulting from the different density layers.

We performed indentation measurements and synchrotron nanotomography of a single lens after inducing cracks in it by mechanical cutting (*15*). From the indentation experiments, we could derive the values of the elastic constants and the hardness (table S4). To estimate the (mode I) fracture toughness K_{IC} of the samples, we used the classical Lawn, Evans, and Marshall model (*15*, *27*, *28*). Although this model was primarily developed for polycrystalline materials, the comparison of K_{IC} of various single crystals is possible. We performed the indentation measurements on the uppermost polished surface of the lenses, which corresponds to the [001] crystallographic direction of calcite, and hence we could compare our results to those obtained for [001]-cut and polished geological calcite. We found that the K_{IC} in brittlestar lens increased by more than twofold (2.21) relative to the geological counterpart, from 0.19 ± 0.06 to 0.42 ± 0.08 MPa·$m^{1/2}$ (table S5). These values are of the same order as those determined for geological calcite (*29*) (table S5), although the absolute values obtained in different studies cannot be rigorously compared. The indentation trace shows a layering structure, which is not observed in the geological counterpart (fig. S10) and is probably a result of cracks that propagate parallel to the alternating layers observed in Figs. 1F and 4, A, B, and D. Indentation on the heat-treated lenses (fig. S11) demonstrated that after annealing, the hardness (table S4) and the fracture toughness (table S5) decreased by 50 and 25%, respectively, as expected. The fracture toughness after annealing is nevertheless 1.63 times that of geological calcite.

Nano–computed tomography (nanoCT) of a single lens revealed that the lens has several alternating layers of density (indicated by the brightness in phase contrast in Figs. 1F and 4D).

The alternating densities are probably due to the different concentrations of magnesium-rich nanoprecipitates that coincide with the diffraction-mapping features. A varying density of nanoprecipitates results in varying degrees of compressive stresses in the lens, as indicated by the scanning diffractometry (Fig. 4, A and B). We would expect, then, a propagating crack to become more retarded and more deflected as the compressive stresses increase. Figure 4D (inset) shows that the crack indeed deflects each time it approaches a varying-density layer. Such crack deflection thus provides further evidence of enhanced toughness owing to the Guinier–Preston–like precipitates within the matrix; however, the layered structure can also contribute to the enhancement in mechanical properties (*30*). It should be emphasized that Guinier–Preston zones in metals lead to an increase in hardness, strength, and brittleness by mitigating dislocation motion, whereas in biogenic calcite, hardness, strength, and toughness are simultaneously enhanced by a different mechanism: namely, mitigation of cracks.

By considering the average crack deflection length $a_{=} = 300$ to 500 nm (along the layer interfaces of thickness $t \cong 250$ nm; see fig. S12) in combination with the measured compressive strain and calculated compressive stress $\sigma_0 \sim -170$ MPa in the matrix, we have developed a model to estimate the toughening $\frac{K^*_{IC}}{K_{IC}}$, resulting in

$$\frac{K^*_{IC}}{K_{IC}} = (1 - \sigma_0/\sigma_C)\sqrt{1 + ka_{=}/t}$$

where σ_C is the material strength in the absence of precompression and k represents the ratio between mode II and mode I fracture energies, assumed to be close to unity (*15*). From the measured toughening of the heated lenses (1.63, only due to crack deflection) and natural lenses (2.21, due to crack deflection and precompression), we estimate $a_{=} \sim 415$ nm (in agreement with the observations; see fig. S12) and $\sigma_C = 472$ MPa. Thus, the strength of the natural lenses $\sigma_C = \sigma_C - \sigma_0 = 642$ MPa demonstrates a strengthening only due to precompression of 1.36. The measured toughening of 2.21 and estimated strengthening of 1.36 represent a considerable simultaneous increase in both the fracture toughness and strength of calcite, the latter of which is typically on the order of a few tens of megapascals for macroscopic geological calcite (*31*).

Although there are some known examples of biogenic crystals under compression (*32*, *33*), the strategy described here provides an elegant way to maintain a solid matrix under compressive strains, known to be among the most efficient means of toughening ceramics such as tempered glass or prestressed concrete. The nanometric size of the precipitates enables them to bear the high tensile stresses. Another appealing aspect of this system is its ability to achieve a superior microstructure at ambient temperature and pressure as a result of its formation via supersaturated amorphous transient precursor rather than via heating and quenching, as in conventional materials science.

REFERENCES AND NOTES

1. A. H. Heuer *et al*., *Science* **255**, 1098–1105 (1992).
2. L. M. Gordon *et al*., *Science* **347**, 746–750 (2015).
3. J. A. Raven, A. H. Knoll, *Geomicrobiol. J.* **27**, 572–584 (2010).
4. R. Blakemore, *Science* **190**, 377–379 (1975).
5. J. C. Weaver *et al*., *Science* **336**, 1275–1280 (2012).
6. V. C. Sundar, A. D. Yablon, J. L. Grazul, M. Ilan, J. Aizenberg, *Nature* **424**, 899–900 (2003).
7. L. Li *et al*., *Science* **350**, 952–956 (2015).
8. A. Herman, L. Addadi, S. Weiner, *Nature* **331**, 546–548 (1988).
9. P. Fratzl, R. Weinkamer, *Prog. Mater. Sci.* **52**, 1263–1334 (2007).
10. A. R. Studart, *Adv. Funct. Mater.* **23**, 4423–4436 (2013).
11. E. Beniash, J. Aizenberg, L. Addadi, S. Weiner, *Proc. R. Soc. London Ser. B* **264**, 461–465 (1997).
12. Y. Politi, T. Arad, E. Klein, S. Weiner, L. Addadi, *Science* **306**, 1161–1164 (2004).
13. N. Vogel *et al*., *Proc. Natl. Acad. Sci. U.S.A.* **112**, 10845–10850 (2015).
14. O. B. M. Hardouin Duparc, *Metall. Mater. Trans. A Phys. Metall. Mater. Sci.* **41**, 1873–1882 (2010).
15. Materials and methods and supplementary text are available as supplementary materials.
16. J. Aizenberg, A. Tkachenko, S. Weiner, L. Addadi, G. Hendler, *Nature* **412**, 819–822 (2001).
17. G. Hendler, M. Byrne, *Zoomorphology* **107**, 261–272 (1987).
18. E. Zolotoyabko *et al*., *Cryst. Growth Des.* **10**, 1207–1214 (2010).
19. B. Pokroy *et al*., *J. Struct. Biol.* **155**, 96–103 (2006).
20. R. I. Harker, O. F. Tuttle, *Am. J. Sci.* **253**, 274–282 (1955).
21. P. Fratzl, O. Penrose, J. L. Lebowitz, *J. Stat. Phys.* **95**, 1429–1503 (1999).
22. T. Mori, K. Tanaka, *Acta Metall.* **21**, 571–574 (1973).
23. B. Pokroy, E. Zolotoyabko, *Chem. Commun. (Camb.)* **16**, 2140–2142 (2005).
24. P. N. T. Unwin, G. W. Lorimer, R. B. Nicholson, *Acta Metall.* **17**, 1363–1377 (1969).
25. S. M. Wise, J. S. Kim, W. C. Johnson, *Thin Solid Films* **473**, 151–163 (2005).
26. B. Aichmayer, P. Fratzl, S. Puri, G. Saller, *Phys. Rev. Lett.* **91**, 015701 (2003).
27. B. Lawn, R. Wilshaw, *J. Mater. Sci.* **10**, 1049–1081 (1975).
28. A. G. Evans, E. A. Charles, *J. Am. Ceram. Soc.* **59**, 371–372 (1976).
29. M. E. Kunitake, L. M. Mangano, J. M. Peloquin, S. P. Baker, L. A. Estroff, *Acta Biomater.* **9**, 5353–5359 (2013).
30. O. Kolednik, J. Predan, F. D. Fischer, P. Fratzl, *Adv. Funct. Mater.* **21**, 3634–3641 (2011).
31. D. Grady, R. Hollenbach, *Geophys. Res. Lett.* **6**, 73–76 (1979).
32. B. Pokroy, V. Demensky, E. Zolotoyabko, *Adv. Funct. Mater.* **19**, 1054–1059 (2009).
33. J. B. Forien *et al*., *Nano Lett.* **15**, 3729–3734 (2015).

ACKNOWLEDGMENTS

Helpful scientific discussions with P. Fratzl are acknowledged with thanks. We also thank M. Kalina for help in preparing the TEM samples and M. D'Incau and H. Gourkar (Anton-Paar Pvt. Ltd. India) for help during some of the microindentation experiments. The x-ray diffraction and nanoCT measurements described in this paper were carried out at beamlines ID13, ID22, and ID16B of the European Synchrotron Radiation Facility (Grenoble, France). This work was primarily supported by the Alon Fellowship for Outstanding Young Researchers of the Israeli Council for Higher Education (B.P.) and the RBNI Technion. N.M.P. is supported by the European Commission H2020 under the Graphene Flagship Core 1 no. 696656 (WP14 "Polymer Composites"), under the Future and Emerging Technologies Proactive "Neurofibres" no. 732344, and by Fondazione Caritro under "Self-Cleaning Glasses" no. 2016.0278 to L.K. P.U.P.A.G. acknowledges NSF grant DMR-1603192 and U.S. Department of Energy (DOE) grant DE-FG02-07ER15899. PEEM experiments were done at the Advanced Light Source, which is a DOE Office of Science User Facility supported by grant DE-AC02-05CH11231. The geological dolomite sample was provided courtesy of R. Slaughter (Univ. of Wisconsin, Geology Museum).

SUPPLEMENTARY MATERIALS

www.sciencemag.org/content/358/6368/1294/suppl/DC1
Materials and Methods
Supplementary Text
Figs. S1 to S12
Tables S1 to S5
Movie S1
References (*34*–*54*)

22 September 2016; resubmitted 16 March 2017
Accepted 27 September 2017
10.1126/science.aaj2156

Coherently aligned nanoparticles within a biogenic single crystal: A biological prestressing strategy

Iryna Polishchuk, Avigail Aronhime Bracha, Leonid Bloch, Davide Levy, Stas Kozachkevich, Yael Etinger-Geller, Yaron Kauffmann, Manfred Burghammer, Carlotta Giacobbe, Julie Villanova, Gordon Hendler, Chang-Yu Sun, Anthony J. Giuffre, Matthew A. Marcus, Lakshminath Kundanati, Paul Zaslansky, Nicola M. Pugno, Pupa U. P. A. Gilbert, Alex Katsman and Boaz Pokroy

Science **358** (6368), 1294-1298.
DOI: 10.1126/science.aaj2156

Many roads to being tough

A number of routes exist to increase toughness in both natural and human-made materials—for example, using secondary phases and precipitates or exploiting tailored architectures and shaped crystals. Polishchuk *et al.* detail the nanoscale internal structure of calcitic microlenses formed by a brittlestar (see the Perspective by Duffy). The segregation of magnesium-rich particles forms a secondary phase that places compressive stresses on the host matrix. This toughening mechanism resembles Guinier-Preston zones known in classical metallurgy.

Science, this issue p. 1294 see also p. 1254